

Calculation of tunneling current across Trapezoidal potential barrier in a Scanning Tunneling Microscope*

Malati Dessai[†] and Arun V Kulkarni[‡]

*Department of Physics,
Birla Institute of Technology and Science-Pilani,
K K Birla Goa campus, Goa, 403726.*

(Dated: October 5, 2022)

The Planar Model of the Electrode-Vacuum-Electrode configuration for STM in which electrode surfaces are assumed to be infinite parallel planes, with atomic size separation and vacuum between them, is used to calculate tunneling current densities for both low and high bias voltages. Non WKB, Airy function solutions for the Schrödinger Equation for the trapezoidal barrier in the tunneling region are used to calculate the tunneling probability. Temperature dependent Fermi Factors for each electrode are introduced and the calculation involves integration over the electron energies. In order to convert the current densities obtained in the planar model to tunneling currents the tip and sample surfaces are modelled as confocal hyperboloids, and the tip sample distance is replaced by the length of the line of force (field line). The current is found by integrating the current density over a finite area of the tip. The calculated tunnel currents for a few electrode pairs at room temperature are plotted for several values of bias voltage, tip sample distances, and tip radii of curvature. Pauli Effects are studied as a function of bias voltage and tip-sample distance. Some estimate of lateral resolution and its dependence on bias voltage and tip radius is also presented.

Keywords: Tunneling; Tunnel junctions; Trapezoidal barrier; confocal hyperboloids; Electrode-vacuum-Electrode.

INTRODUCTION

Scanning Tunneling Microscopes (STM's) allow imaging of surface structures with atomic scale resolution and have been the workhorses for most surface science studies in recent decades. Scanning probe microscopes usually involve a sharp tip brought close to a sample which is mostly flat except for atomic

scale surface features. The atoms of the tip interact with those of the sample and in case of the STM this interaction causes tunnelling of the electrons between the tip and the sample. An experimentally measurable quantity such as the tunneling current is measured as a function of the tip sample distance and the bias potential between tip and sample. In typical STM applications, extremely sharp tips are used and further a very close proximity between the tip and sample is maintained. As a result, the tip-sample interaction is highly localized and the tunneling current is sensitive only to the local surface properties of the sample. This sensitivity is further enhanced due to the STM current having an almost exponential dependence on the tip-

* Corresponding author. Arun V. Kulkarni Tel.:0832 2580309; fax: +91-8322557033 E-mail address: avkbits@goa.bits-pilani.ac.in

[†] Also at Department of Physics, Parvatibai Chowgule College of Arts and Science, Margao, Goa, 403602.

[‡] avkbits@goa.bits-pilani.ac.in

sample distance, thus achieving atomic scale resolution[1]. Since the tunneling is a very sensitive function of the tip sample distance, the measured values of the tunnel current almost resemble the sample surface topography when raster scanning of the sample is carried out by the tip.

There are several other works in literature, that calculate tunneling current density such as Simmons[2], Hartman and Chivian[3] in which the WKB approximation is used for calculating the tunneling probability. While tunneling current densities are not directly experimentally measurable tunneling currents are directly measurable and these are of particular interest in comparing theory with experiment.

Tersoff and Hamann[4] have developed a formalism starting from Bardeen's theory[5][6] to calculate tunneling currents. However, their calculations is likely to work best for very low tip-sample distances and also for very low biases. In this paper the tip-sample distances exceed this limit and range from a few Å to 20 Å. The calculation of Chen et.al.[7] uses Bessel functions of one-third order and therefore goes beyond the WKB approximation. However only the current densities are reported and effects of Pauli Blocking are not investigated. The self consistent calculation of Banerjee et.al.[8] uses the WKB approximation. They have not studied Pauli Blocking effects and also report only current densities and not currents.

The tip and sample here are initially treated as plane surfaces. In this so called planar model, only tunneling current densities and not tunneling currents can be calculated. The latter would be infinity in a planar model. In the non planar model considered here, the tip and the sample are modelled as confocal surfaces in a prolate spheroidal co-ordinate system. In this paper the tunneling current densities are converted into currents through a method described by Saenz and Garcia[9].

The energies of electrons inside the electrodes are distributed according to the Fermi-Dirac distribution. With these assumptions the tunneling current density and tunneling currents through the barrier are calculated for both high and low bias voltages.

THEORY

A. CURRENT DENSITY AND FERMI FACTOR

Consider two plane conducting electrodes with infinite plane surfaces, separated by vacuum whose width ranges from 2 Å to 20 Å. The electrode surfaces are initially assumed to be of infinite area. With this assumption, both the Laplace equation for the electrostatic potential, and the Schrödinger equation with this potential, reduce to one dimensional equations.

Let a bias potential V_b be applied across the electrodes. Let η_1 , ϕ_1 , η_2 , ϕ_2 , be the Fermi energies and work functions of the left (first) electrode and the right (second) electrode respectively (Fig.1a). The left electrode (electrode 1) is assumed to be at higher potential than the right electrode (electrode 2) so that the electric field points along the negative x axis, and if a free electron were introduced between electrodes it would experience a force along the positive x axis as shown in Fig.2. Tunneling of electrons between the two plane surfaces occurs through the effective trapezoidal barrier in the vacuum region. The case for zero bias between dissimilar electrodes is shown in Fig.1a. The barrier potential in this case is the difference ($\phi_1 - \phi_2$) between the work functions of the two conducting electrodes. When biased, the barrier potential in the vacuum region, is the sum of the contact potential ($\phi_1 - \phi_2$) and the applied external bias eV_b as shown in Fig.1b. Forward electron current density is along the positive x axis and reverse electron current density is along the negative x axis.

The connection between the tunneling

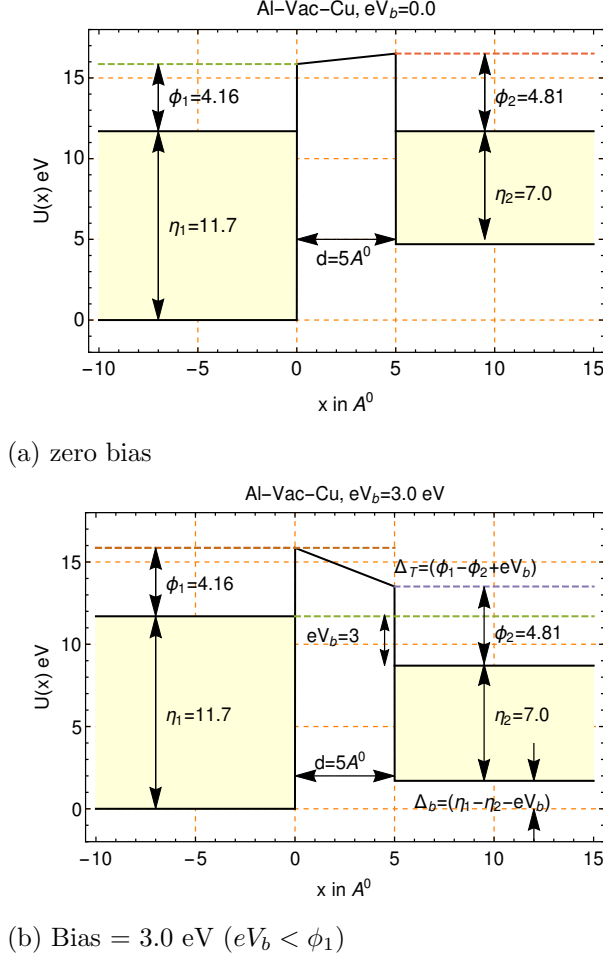


FIG. 1: Dissimilar Electrodes with vacuum barrier at a) Zero Bias b) Bias = 3.0 eV

current density and the probability of tunneling through the barrier, is well established and the earliest accounts of it are by Fowler and Nordheim[10] and Simmons[2][11]. In these accounts, one of the principal assumptions is that the number of electrons that can occupy a unit volume in the 6 dimensional phase space is $\frac{2}{h^3}$, and therefore the number per unit volume (of coordinate space) of electrons in the velocity space volume element $d^3v = dv_x dv_y dv_z$ about the velocity vector \mathbf{v} is $\mathbf{n}(v)d^3v = \frac{2m}{h^3}d^3v$. The energy of these electrons is

$$E = \frac{1}{2}m\mathbf{v}^2 = \frac{1}{2}m(v_x^2 + v_y^2 + v_z^2) = E_x + E_y + E_z \quad (1)$$

where $E_x = \frac{1}{2}mv_x^2$, $E_y = \frac{1}{2}mv_y^2$, $E_z = \frac{1}{2}mv_z^2$ are the kinetic energies of the electrons for translational motion along the x , y , and z directions respectively. The number density of electrons in the electrode 1 that are available for tunneling would be $n_1 d^3v = \mathbf{n}(v)f_1(E) d^3v$ where $f_1(E) = [1 + \exp(\beta(E - \eta_1))]^{-1}$ is the Fermi Dirac Distribution function which can be regarded as the probability of occupation of the energy level E in the electrode 1. Note $\beta = \frac{1}{kT}$ where k is the Boltzmann Constant and T is the temperature (in Kelvin) of both the electrodes.

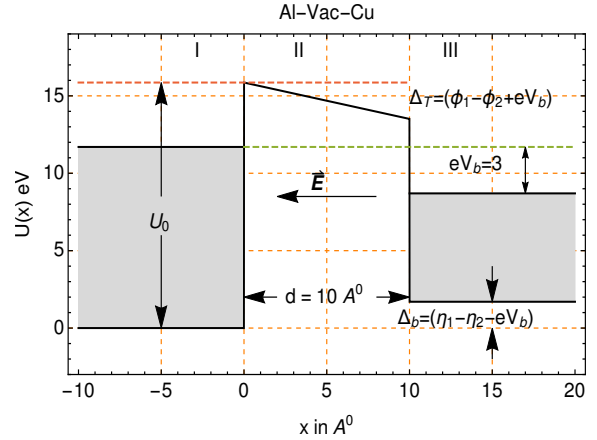


FIG. 2: Electrode 1 is at higher potential ($U_0 = \eta_1 + \phi_1$) and the electric field points along the negative x axis

The number density of electrons that can tunnel through the barrier is

$$n_T(v)d^3v = n_1(v)D(E_x)d^3v$$

where $D(E_x)$ is the probability of tunneling through the barrier. In theoretical calculation

$$D(E_x) = |T(E_x)|^2 \frac{j_{out}}{j_{inc}}$$

where T is the transmission amplitude for tunneling through the barrier and if plane wave solutions are used within the electrodes then $j_{inc} = \frac{\hbar k_1}{m}$ and $j_{out} = \frac{\hbar k_2}{m}$ for forward currents. where $\hbar k_1$ and $\hbar k_2$ are x -components

of the momenta of the electrons in the first and the second electrodes.

$$\hbar k_1 = \sqrt{2mE_x}, \quad \hbar k_2 = \sqrt{2m(E_x - \Delta_B)} \quad (2)$$

where E_x is the kinetic energy of motion of the electrons in the x - direction. For reverse currents $j_{inc} = \frac{\hbar k_2}{m}$ and $j_{out} = \frac{\hbar k_1}{m}$. Note that the transmission amplitude is independent of the direction of tunneling. Hence it is the same for both forward and reverse tunneling currents. Not all of the electrons emitted by electrode 1 will necessarily be accepted by the electrode 2, since there will be partial occupation of this level by electrons already present in the electrode 2. This is due to the Pauli Exclusion Principle and may be called the Pauli Effect. Others[2][12][13][14] have referred to this phenomena as Pauli Blocking.

To obtain the number density of electrons in the energy level E , that are accepted by the electrode 2, one must multiply n_T by the probability of vacancy of this energy level, in the electrode 2. This is given by $[1 - f_2(E + \Delta_b)]$ where

$$f_2(E + \Delta_b) = [1 + \exp(\beta(E + \Delta_b - \eta_2))]^{-1}$$

The energy argument in the Fermi Dirac function for electrode 2 will be shifted by $+\Delta_b = \eta_1 - \eta_2 - eV_b$, because the zero level of the energy in electrode 2 is shifted by $-\Delta_b$ compared to that of the electrode 1. But as can be seen from Figures 2 and 6

$$(E + \Delta_b - \eta_2) = (E + eV_b - \eta_1)$$

Therefore

$$f_2(E + \Delta_b) = f_1(E + eV_b)$$

Thus the number density of electrons that will be found in the states of electrode 2, and which contribute to the forward current are

$$\begin{aligned} & n_{\text{For}} d^3v \\ &= \frac{2m^3}{h^3} \frac{k_2}{k_1} |T(E_x)|^2 f_1(E) [1 - f_2(E + \Delta_b)] d^3v \end{aligned} \quad (3)$$

$$= \frac{2m^3}{h^3} \frac{k_2}{k_1} |T(E_x)|^2 f_1(E) [1 - f_1(E')] d^3v \quad (4)$$

where $E' = E + eV_b = E_x + E_r + eV_b$. The forward current density is then

$$J_{\text{For}} = e \int v_x n_{\text{For}} d^3v$$

Now $v_x dv_x = (dE_x/m)$ and

$$dv_y dv_z = v_r dv_r d\theta = (dE_r/m) d\theta$$

where the y, z velocity components are expressed in terms of their polar components (v_r, θ) in the $y - z$ plane. Also $E_r = \frac{1}{2}mv_r^2$ and $E = E_x + E_r$. Putting it all together and integrating over θ gives

$$J_{\text{For}} = \frac{4\pi me}{h^3} \int dE_x \frac{k_2}{k_1} |T(E_x)|^2 \times \int_0^\infty dE_r f_1(E) [1 - f_1(E')] \quad (5)$$

In a like manner one can also calculate the reverse current density to be

$$J_{\text{Rev}} = \frac{4\pi me}{h^3} \int dE_x \frac{k_1}{k_2} |T(E_x)|^2 \times \int_0^\infty dE_r [1 - f_1(E)] f_1(E') \quad (6)$$

The net current density is given by $J_{\text{Net}} = J_{\text{For}} - J_{\text{Rev}}$, which becomes

$$\begin{aligned} J_{\text{Net}} &= \frac{4\pi me}{h^3} \int dE_x |T(E_x)|^2 \times \\ &\int_0^\infty dE_r \left[f_1(E) [1 - f_1(E')] \frac{k_2}{k_1} - \right. \\ &\quad \left. [1 - f_1(E)] f_1(E') \frac{k_1}{k_2} \right] \end{aligned} \quad (7)$$

Define the Fermi Factor $\mathcal{F}(E_x)$ as

$$\begin{aligned} \mathcal{F}(E_x) &= \int_0^\infty dE_r \left[f_1(E) [1 - f_1(E')] \frac{k_2}{k_1} - \right. \\ &\quad \left. [1 - f_1(E)] f_1(E') \frac{k_1}{k_2} \right] \end{aligned} \quad (8)$$

Carrying out the integral over E_r

$$\mathcal{F}(E_x) = \frac{k_2}{k_1} F_1(E_x) - \frac{k_1}{k_2} F_1(E_x + eV_b) + \frac{\left[\frac{k_1}{k_2} - \frac{k_2}{k_1}\right]}{(1 - e^{-\beta eV_b})} \left[F_1(E_x + eV_b) - e^{-\beta eV_b} F_1(E_x) \right] \quad (9)$$

where

$$F_1(E_x) = \frac{1}{\beta} \text{Log}[1 + e^{-\beta(E_x - \eta_1)}]$$

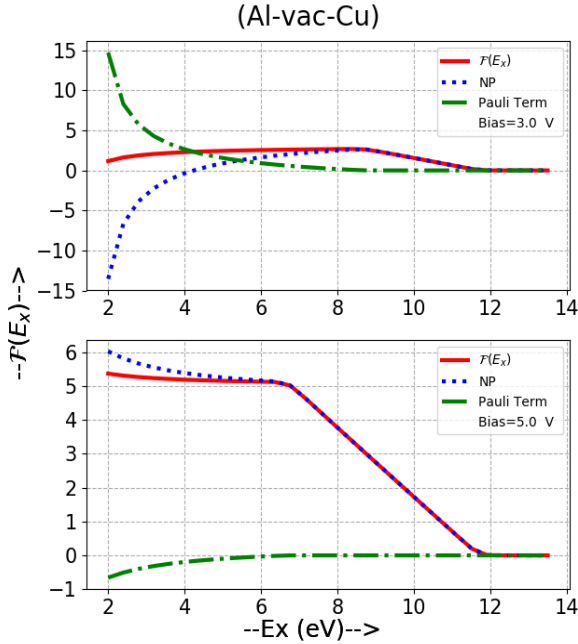


FIG. 3: Fermi Factor for Bias voltage of 3 and 5 V for Al-vac-Cu. The solid red line refers to $\mathcal{F}(E_x)$, the dotted line refers to Non-Pauli term, and dot-dashed line refers to Pauli term.

The first two terms are the Non-Pauli contribution; these are the terms that one would get if Pauli Blocking were completely ignored. The third term in equation (9) explicitly introduces Pauli Effects. The behaviour of these terms *viz* Non-Pauli, $\mathcal{F}(E_x)$, and the Pauli term (third term only), as a function of E_x is displayed in Fig.3. The Fermi Function $\mathcal{F}(E_x)$ (solid red line) is seen to peak at

$8.7 \text{ eV} \approx \eta_1 - eV_b$ for $eV_b = 3 \text{ eV}$; and it peaks at $6.7 \text{ eV} \approx \eta_1 - eV_b$ for $eV_b = 5 \text{ eV}$. Subsequently $\mathcal{F}(E_x)$ is found to decrease rapidly to zero as E_x exceeds η_1 . This is found true for all bias voltages. The dotted line refers to the Non-Pauli(NP) term, which may have negative values for low bias voltages. For these voltages the reverse current exceeds the forward current. This may be due to the different flux ratios for the forward and the reverse currents. The dot-dashed line refers to the third term of equation (9). The third term is seen to go to zero at about $E_x = \eta_1 - eV_b$. This term contains Pauli Effects and it is studied in more detail in Figures 4 and 5.

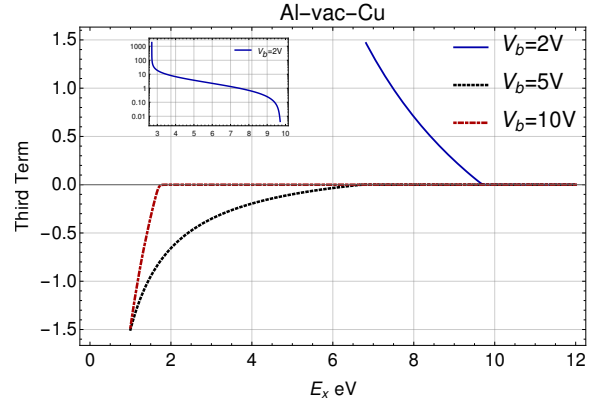


FIG. 4: Third Term as a function of E_x for bias voltages 2V, 5V, and 10V for Al-vac-Cu.

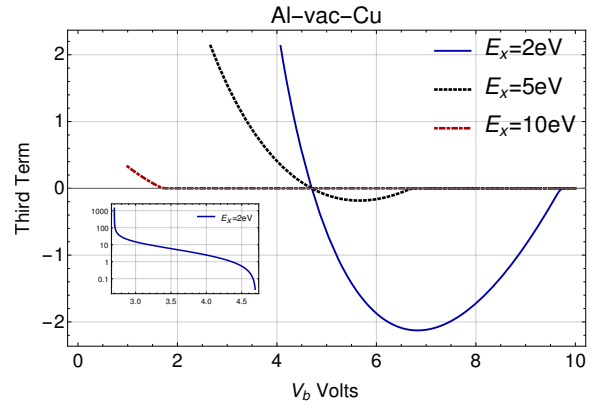


FIG. 5: Third Term as a function of V_b for electron energies of 2eV, 5eV, and 10eV for Al-vac-Cu.

Figure 4 plots the third term for fixed bias voltages ($V_b = 2\text{V}$, $V_b = 5\text{V}$, $V_b = 10\text{V}$) as a function of electron energies in the range (1 eV to 12 eV). The graph shows that Pauli Effects are significant for low energy electrons and especially for low bias voltages. For $E_x > \eta_1 - eV_b$ the third term is essentially zero implying that there is negligible Pauli Effect. The inset in this figure shows the third term for 2V rising rapidly by at least 4 orders of magnitude for very low values of E_x . Figure 5 plots the third term for fixed electron energies ($E_x = 2\text{eV}$, $E_x = 5\text{eV}$, $E_x = 10\text{eV}$) as a function of the bias voltage in the range (1V to 10V). The inset in this figure shows the third term for $E_x = 2\text{eV}$ rising rapidly by at least 3 orders of magnitude for very low values of bias voltage. All curves in Fig.5 pass through zero at $eV_b = \eta_1 - \eta_2$ which in case of electrodes Al and Cu is given by $V_b = 4.7\text{ V}$. This is because $k_1 = k_2$ for this value of bias, and the zero level of the energy in the two electrodes become identical. For bias voltages lesser than $eV_b = \eta_1 - \eta_2$ the third term is positive and its effect is to increase the net tunneling current beyond the non-Pauli contribution. For bias voltages larger than this value the third term becomes negative and the Pauli Effect will be to reduce the net tunneling current from its Non-Pauli value.

The net current density becomes

$$J_{\text{Net}} = \frac{4\pi me}{h^3} \int_{E_x^{\min}}^{E_x^{\max}} dE_x |T(E_x)|^2 \mathcal{F}(E_x) \quad (10)$$

where the limits of the integral in equation (10) are given by

$$E_x^{\min} = \text{Max}[0, \Delta_b] \text{ and } E_x^{\max} = \eta_1 + \phi_1$$

E_x^{\min} is the minimum of energy in the energy Stage I and E_x^{\max} is the maximum of energy in the energy Stage II. The energy stages I, II, and III are described in the next section.

B. TUNNEL AMPLITUDE $T(E_x)$

Let the two planar electrodes described in the previous section be parallel to each other and parallel to the y-z plane. Let their surfaces be at $x = 0$ and $x = d$ respectively, with the intervening space being occupied by vacuum. The entire extent of the x-axis can be divided up into three spatial regions and the potential energy of an electron in these three regions is given by

$$U(x) = \begin{cases} 0 & x < 0 \\ U_{II}(x) & 0 \leq x \leq d \\ \Delta_b & x > d \end{cases} \quad (11)$$

where

$$U_{II}(x) = (\eta_1 + \phi_1) - (\phi_1 - \phi_2 + eV_b) \frac{x}{d} \quad (12)$$

The wavefunctions in two regions ($x < 0$) and ($x > d$) are given by

$$\psi_1(x) = e^{ik_1x} + Re^{-ik_1x}, \quad x < 0 \quad (13)$$

$$\psi_3(x) = Te^{ik_2x}, \quad x > d \quad (14)$$

where, R , T are the reflection and transmission amplitudes. The wavefunction ψ_b in the barrier region $0 \leq x \leq d$ is given by the Schrödinger equation for the linear (trapezoidal) potential

$$\frac{d^2\Psi_b}{dx^2} - (A - Bx)\Psi_b = 0 \quad (15)$$

where

$$A = \frac{2m}{\hbar^2}(\eta_1 + \phi_1 - E_x) \quad (16)$$

$$B = \frac{2m}{\hbar^2 d}(\phi_1 - \phi_2 + eV_b) \quad (17)$$

If the electrodes were at absolute zero temperature, only electrons at the Fermi levels of the electrodes would undergo tunneling. At higher temperatures, electrons with a wider range of energies will be involved in tunneling. The energy range of such electrons can be divided into three Energy Stages. Fig.6 shows the three Energy Stages for Al-vac-Cu

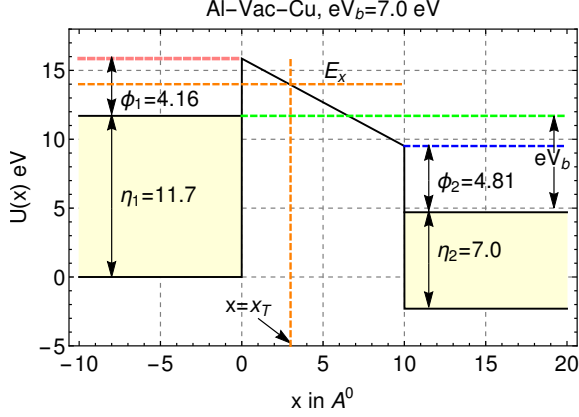


FIG. 6: Energy Stages I (0 eV to 9.51 eV), II (9.51 eV to 15.86 eV), and III (> 15.86 eV) for Al-vac-Cu, and $eV_b = 7.0$ eV ($eV_b > \phi_1$). The upper limits are indicated by blue dotted line (Stage I), pink dotted line (Stage II).

system for which $\eta_1 = 11.7$ eV, $\phi_1 = 4.16$ eV, $\eta_2 = 7.0$ eV, $\phi_2 = 4.81$ eV, $V_b = 7$ volts.

Energy Stage I: The barrier region in this stage does not contain a turning point. The energy in this region ranges from $\text{Max}[0, \Delta_b] < E_x < (\eta_1 + \phi_1 - eV_b)$. Therefore, the term $(A - Bx)$ will never be zero $\forall x \in [0, d]$.

Energy Stage II: In this stage, there is a turning point inside the barrier region at $x = x_T = \frac{A}{B}$. The energy range in this stage is $(\eta_1 + \phi_2 - eV_b) < E_x < (\eta_1 + \phi_1)$ as shown in Fig.6. The barrier is triangular and electrons tunneling out of this triangular barrier are real (not virtual) electrons which have not entered the the second electrode and those that do so enter the second electrode, contribute to the tunneling current.

Energy Stage III: The energy of the electrons in this stage exceeds $(\eta_1 + \phi_1)$ and these electrons should be emitted without having to tunnel through any barrier suggesting that the transmission probability would be very high. However for most values of ϕ_1 the electron energy is so far above the Fermi energy η_1 that the Fermi factor (for room temperatures) is essentially zero and the contribution of electrons in this energy stage

at these temperatures to the current density is vanishingly small. Therefore unless the electrode temperatures are very high (i.e. comparable to the Fermi temperature of the electrodes), the contribution of electrons in this Energy Stage will be neglected altogether.

In Energy Stages I and II the Schrödinger equation (4) reduces to the Airy equation.

$$\frac{d^2 \Psi_b}{dh^2} - h \Psi_b = 0 \quad (18)$$

where $h = h(x) = \frac{A}{B^{2/3}} - B^{1/3}x$. The general solution of the Airy Differential equation can be written as [15]

$$\psi_b(x) = C\phi^{(1)}(x) + D\phi^{(2)}(x) \quad (19)$$

where

$$\phi^{(1)}(x) = \frac{Ai[h(x)]}{Ai[h(\bar{x})]} \quad \phi^{(2)}(x) = \frac{Bi[h(x)]}{Bi[h(\bar{x})]} \quad (20)$$

The denominator of the functions $\phi^{(1)}$ and $\phi^{(2)}$ contain Airy functions evaluated at \bar{x} (a fixed value of x near the centre of the barrier region). These denominators are sometimes required to avoid overflow and underflow errors in the calculation of the wavefunctions for different values of x in the barrier. The constants C and D are determined from matching of the wavefunction and its derivative at the relevant spatial boundaries. In Energy Stage I these boundaries are at $x = 0$ and $x = d$. In Energy Stage II, two separate wavefunctions ψ_{b1} and ψ_{b2} have to be determined for $x < x_T$, and $x > x_T$ respectively. The spatial boundaries for the former are at $x = 0$ and $x = x_T$ and that for the latter, are at $x = x_T$ and $x = d$. The Tunneling amplitude is given by

$$T(E_x) = e^{-ik_2d} \begin{cases} \psi_b(d) & \text{in Stage I} \\ \psi_{b2}(d) & \text{in Stage II} \end{cases} \quad (21)$$

Fig.7 shows that the $|T(E_x)|^2$ increases with E_x which is to be expected.

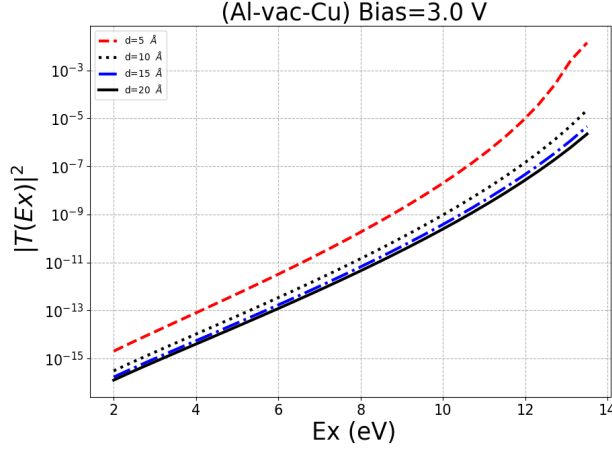


FIG. 7: Plot of Transmission Probability versus E_x for Bias Voltage = 3 V & $d = 5, 10, 15, 20 \text{ \AA}$

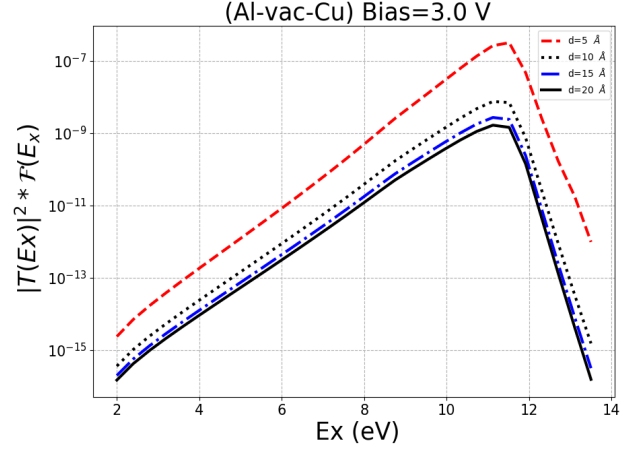


FIG. 8: Plot of product of Transmission Probability and Fermi Factor versus E_x for Bias Voltage = 3 V and $d = 5, 10, 15, 20 \text{ \AA}$

Fig.8, shows a plot of the product of calculated (Airy) $|T(E_x)|^2$ and the Fermi Factor \mathcal{F} for metal electrodes Al(tip) and Cu(sample). The product $|T(E_x)|^2 \times \mathcal{F}$ increases exponentially upto Fermi level ($\eta_1 = 11.7 \text{ eV}$) of the left electrode and drops sharply thereafter, well before reaching the upper limit of Energy Stage II ($\eta_1 + \phi_1 = 15.86 \text{ eV}$). Thus significant contribution to the tunneling current density arises from a narrow energy band (for E_x) around η_1 . The Fermi Factor is thus seen to damp out the contribution to the tunneling current density for larger values of the kinetic energy E_x for the translational motion of the electrons in the x-direction.

Fig.9 compares $|T(E_x)|^2 \times \mathcal{F}$ calculated using Airy functions with that using WKB approximation for an intermediate bias of 3 V. For this bias voltage, this product $|T(E_x)|^2 \times \mathcal{F}$ using the WKB approximation is found to exceed the Airy function determined $|T(E_x)|^2 \times \mathcal{F}$ for low tip-sample distances such as $d = 5 \text{ \AA}$. The two are nearly equal for $d = 10 \text{ \AA}$, however its Airy value exceeds its WKB value for $d = 15 \text{ \AA}$. Thus the WKB approximation does not provide an accurate dependence of the tunnel current densities on the tip-sample distances. This feature suggests that determination of surface topographies of samples would be inaccurate, if the image processing

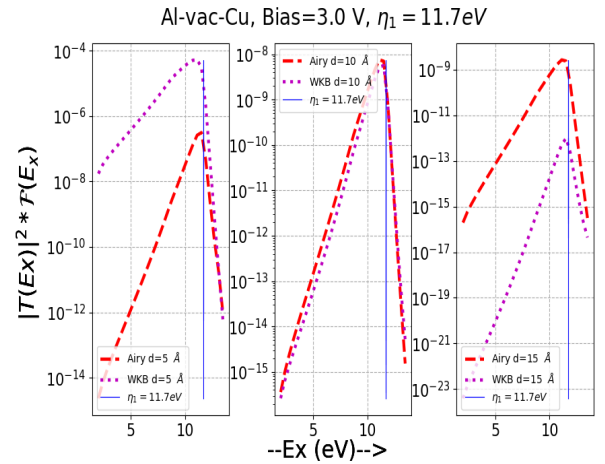


FIG. 9: Plot of Transmission Probability (Airy compared with WKB) versus E_x for Bias Voltage = 3 V and $d = 5, 10 \text{ \AA}$ (Al-vac-Cu).

software uses WKB approximation.

C. $T(E_x)$ FOR VERY LOW BIAS

In the low bias regime (0.1V to 1V) the Airy Function Ai becomes very small causing underflow problems and the Airy function Bi becomes very large causing overflow problems as in the calculation. Even introduction of denominators as in equation (20), doesn't seem to help. Instead it is more use-

ful to convert the Schrödinger equation to the following inhomogeneous equation

$$\mathcal{L}\psi(x) = f(x)\psi(x) \quad (22)$$

where

$$\mathcal{L} = \frac{d^2}{dx^2} - \kappa^2 \quad (23)$$

$$\frac{\hbar^2 \kappa^2}{2m} = \eta_1 + \phi_1 - E_x \quad (24)$$

$$\frac{\hbar^2}{2m} f(x) = -(\phi_1 - \phi_2 + eV_b) \frac{x}{d} \quad (25)$$

The term $f(x)$ in the equation (22), is usually very small for low bias voltages and low contact potentials, permitting a perturbative solution of equation (22).

Fig.8, shows that the maximum contribution to the tunneling occurs for E_x lying in a very narrow energy band whose upper limit is η_1 . For $E_x \leq \eta_1$ the minimum value of $\frac{\hbar^2 \kappa^2}{2m}$ will be ϕ_1 . The condition that $\frac{\hbar^2}{2m}|f(x)|$ be smaller than this minimum value of $\frac{\hbar^2 \kappa^2}{2m}$ is $eV_b < \phi_2$. Hence for low bias voltages, $|f(x)| < \kappa$ is true and perturbative solutions are valid. For $eV_b > \phi_2$ the Airy function methods will do fine.

Define the Green function for the operator \mathcal{L} of equation (23) as

$$\mathcal{L}G(x, x') = \delta(x - x') \quad (26)$$

Let the wavefunction in the barrier region be

$$\psi(x) = \phi_0(x) + \phi(x) \quad (27)$$

where $\phi_0(x)$ is the solution to the homogeneous equation

$$\mathcal{L}\phi_0(x) = 0 \quad (28)$$

From equations (27) and (28), $\phi(x)$ will satisfy

$$\mathcal{L}\phi(x) = f(x) [\phi_0(x) + \phi(x)] \quad (29)$$

$$\begin{aligned} \phi(x') &= \int_0^d G(x, x') f(x) [\phi_0(x) + \phi(x)] dx \\ &+ \text{end point terms} \end{aligned} \quad (30)$$

The end point terms (*viz* at $x = 0$ and $x = d$) can be made to vanish if the Green function and the function ϕ are both made to vanish at $x = 0$ and $x = d$. Equation (30) can be iterated to obtain terms containing higher and higher powers of $f(x)$. Here $f(x)$ will be regarded as small enough to neglect higher than first order terms. Keeping only the first order term, gives

$$\phi(x') = \int_0^d G(x, x') f(x) \phi_0(x) dx \quad (31)$$

and therefore

$$\psi(x) = \phi_0(x) + \int_0^d G(x, x') f(x') \phi_0(x') dx' \quad (32)$$

The tunneling amplitude T^{Gr} is calculated using the wavefunction in equation (32) and joining it smoothly with the wavefunctions given in equations (13) and (14).

For very low bias, the energy of the electrons in the Energy Stage II is well above the Fermi level of the first electrode and the Fermi Factor is extremely small for these energies. Therefore these electrons will make a negligible contribution to tunneling and hence the Green function method outlined above is not extended to the second stage. Instead, the second stage contribution for very low bias voltages is zeroed out.

D. CURRENT FROM CURVED TIPS USING PLANAR MODEL CURRENT DENSITIES

As mentioned in the introduction it is necessary to go beyond the planar model and treat the tip as a sharp pointed surface and let the sample be flat. For a sharp tip, its radius of curvature at the point closest to the sample must be small, so that the length of the electric field lines increases rapidly as one goes away from the centre. Since the tunneling current densities fall off exponentially with increasing electric field line length therefore these current densities when integrated

over the tip area will lead to a finite value for the current.

A good model in which the tip is sharp and the sample is flat is provided by using confocal hyperboloids for the tip and sample shapes (Fig.10). These surfaces are coordinate surfaces in the prolate spheroidal coordinate system[16][17][18][19][9][20][21][22][23]. This is described by

$$x = \rho \cos \phi, \quad y = \rho \sin \phi, \quad z = a\xi\eta \quad (33)$$

where $\rho = a\sqrt{\xi^2 - 1}\sqrt{1 - \eta^2}$, and a is a constant whose value is determined by the tip radius of curvature R and the tip sample distance d as $a = \sqrt{d(d + R)}$. The range of coordinate values are given by

$$1 \leq \xi \leq \infty, \quad -1 \leq \eta \leq 1, \quad 0 \leq \phi \leq 2\pi \quad (34)$$

The Laplace equation for the electrostatic potential in this coordinate system becomes one dimensional and equipotential surfaces are confocal hyperboloids which are a one parameter family of surfaces, whose equation in cartesian coordinates is

$$\frac{z^2}{a^2\eta^2} - \frac{(x^2 + y^2)}{a^2(1 - \eta^2)} = 1 \quad (35)$$

The tip surface (treated here as an emitter) is represented by a hyperboloid described by equation (35) in which $\eta = \eta_{tip} = d/a$. The sample surface is characterised by $\eta = \eta_{sample} = 0$ which is the $x - y$ plane. The equation of the field line that passes through the point (ξ, ϕ) is independent of ϕ and is given by

$$\frac{\rho^2}{a^2(\xi^2 - 1)} + \frac{z^2}{a^2\xi^2} = 1 \quad (36)$$

and the length of this field line stretching from $\eta = \eta_{sample}$ to $\eta = \eta_{tip}$ is

$$d_{fl}(\xi) = a \int_{\eta_{sample}}^{\eta_{tip}} \frac{\sqrt{\xi^2 - \eta^2}}{\sqrt{1 - \eta^2}} d\eta \quad (37)$$

In Fig.10, a small shaded area on the tip is shown along with, a couple of electric field

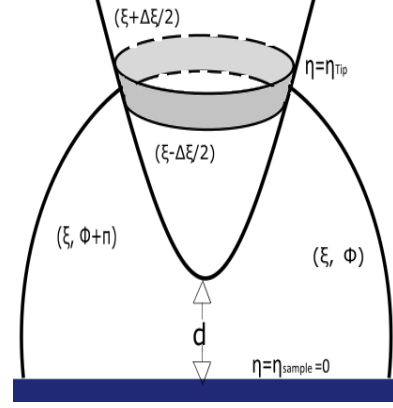


FIG. 10: Hyperboloid Tip and Spheroidal shaped field line.

lines, both lines, parametrized by ξ . This small shaded area on the tip, and the corresponding area on the sample define a planar tunnel junction of infinitesimal area, in which the length of the field line $d_{fl}(\xi)$ plays the role of the tip sample distance. Thus the net current density $J_{Net}(\xi)$ for this infinitesimal area planar tunnel junction is given by equation (10). The product of the area of the shaded region $dS(\xi)$ with the current density of this infinitesimal tunnel junction gives the current carried by it. The sum of these currents for all such junctions covering a reasonably wide area on the tip will give the total net current for the entire non planar tip. Thus planar model current densities can be used to calculate the total net current for a given non planar shape of the tip. This procedure has been well described by Saenz and Garcia [9].

THE CALCULATION

The total current density $J_{Net}(\xi)$ is obtained by integrating the product of the tunneling probability and the Fermi Factor over the energy E_x of the tunneling electrons for the translational motion along the x-direction. The tunneling amplitude $T = T[E_x, d_{fl}(\xi)]$ depends not only upon the energy E_x but also on the location of the point on the tip (dictated by ξ) from where tunneling occurs. The current density $J_{Net}(\xi)$,

given by an equation similar to equation (10) is a function of ξ through its dependence on the length of the field line $d_{fl}(\xi)$, and since $J(\xi)$ decreases rapidly with $d_{fl}(\xi)$ it will also decrease equally rapidly with ξ . The range of energies E_x in the integration spans those in Energy Stages I and II described earlier in section B.

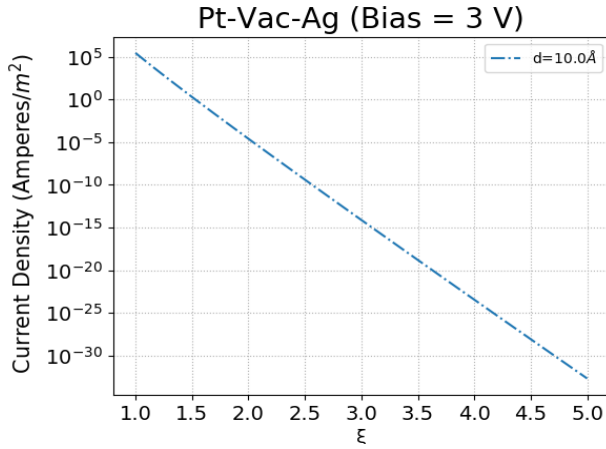


FIG. 11: Plot of Current Density versus Length of field line with $R = 20 A^0$, $d = 10 A^0$ and Bias = 3 V for Pt-vac-Ag

The net current is given by

$$I = \int_1^{\xi_{max}} J(\xi) dS(\xi) \quad (38)$$

where the upper limit ξ_{max} is chosen to have a value of 5, because the current density $J_{Net}(\xi)$ is essentially zero beyond this value as shown in Fig. 11. In this figure it can be seen that the current density drops by roughly 20 orders of magnitude as ξ increases from $\xi = 1$ to $\xi = 5$. The surface element $dS(\xi)$ in equation (38) is given by

$$dS(\xi) = 2\pi a^2 \sqrt{(\xi^2 - \eta_{tip}^2)(1 - \eta_{tip}^2)} d\xi \quad (39)$$

is the area of the shaded region on the tip as shown in Fig. 10. The curved line in this Fig. 10 is the field line corresponding to the parameter ξ ($1 \leq \xi \leq \xi_{max}$).

RESULTS AND DISCUSSION

Figure 12 shows calculated I-V characteristics for identical electrodes (W-vac-W) in which the tip is negatively biased, for several tip-sample distances. The current increases almost exponentially with bias voltage at all distances. Figure 13 shows calculated I-V

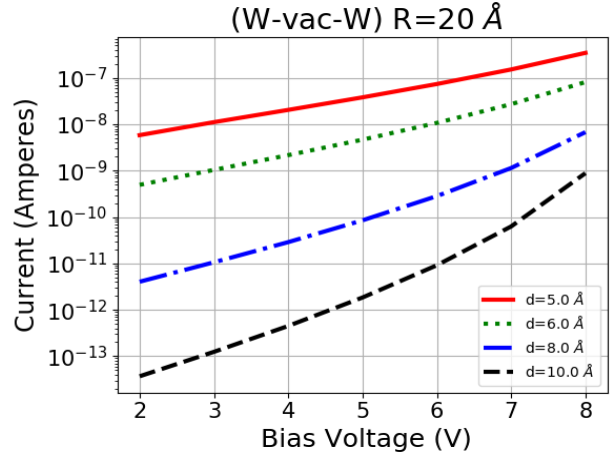


FIG. 12: Plot of Current versus Bias Potential for $R = 20 A^0$ and $d = 5, 6, 8, 10 A^0$ for similar electrodes

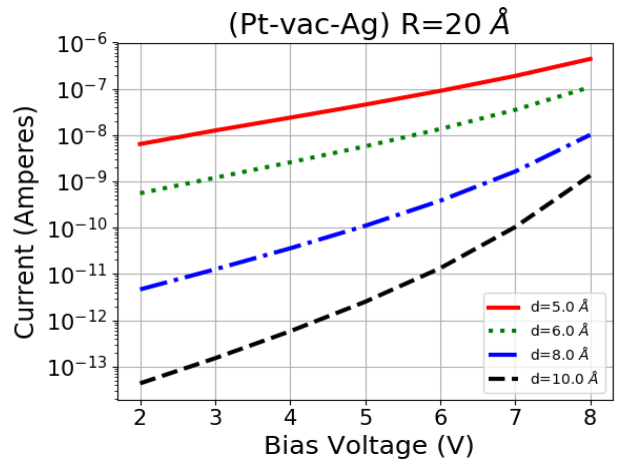


FIG. 13: Plot of Current versus Bias Potential for $R = 20 A^0$ and $d = 5, 6, 8, 10 A^0$ for dissimilar electrodes

characteristics for dissimilar electrodes (Pt-vac-Ag) and the I-V curves behave similar to

the case of identical electrodes, *viz* the current increases almost exponentially with bias voltage for all distances.

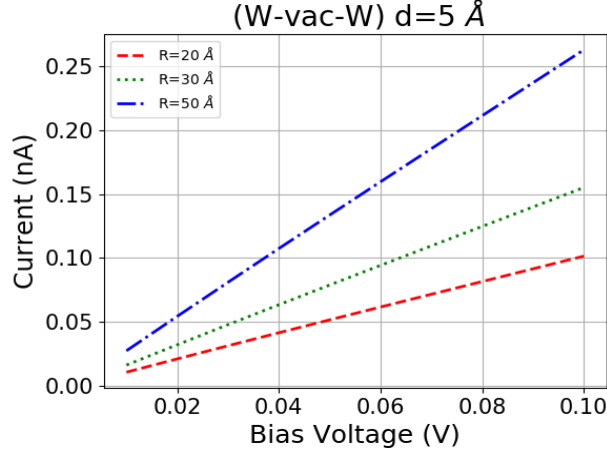


FIG. 14: Plot of Current versus Bias Potential (< 0.1 V) for $R = 20, 30, 50 \text{ Å}$ and $d = 5 \text{ Å}$ for W-vac-W

Ting *et. al.*[24] have reported values of tunneling currents in the W-vac-W electrode system for very low bias voltages and for several cross currents I_{cross} , including for $I_{\text{cross}} = 0$. Here I_{cross} is a current made to flow in the surface of the sample. For $I_{\text{cross}} = 0$, their experimental setup corresponds to the tip-vacuum-sample system for which tunneling currents are calculated in this paper. Tunneling currents of 0.1nA are reported by Ting *et. al.*[24] for low bias voltages in the range [0 to 70 mV]. Fig.14 plots the calculated tunneling current for (W-vac-W) for very low bias for a fixed tip sample distance $d = 5 \text{ Å}$ and several tip radii of curvature ($R = 20, 30, 50 \text{ Å}$). These plots show the tunneling current increasing with the bias voltage as expected. Also the tunneling currents are seen to increase with increasing tip radii. Further for $R = 30 \text{ Å}$, a good numerical agreement with results for $I_{\text{cross}} = 0$ of Ting *et. al.*[24] is obtained.

Figures 15 and 16 show the plots of calculated tunneling currents I versus tip sample distance d in similar (Al-vac-Al) and dissimilar (Pt-Vac-Ag) pairs of electrodes. These

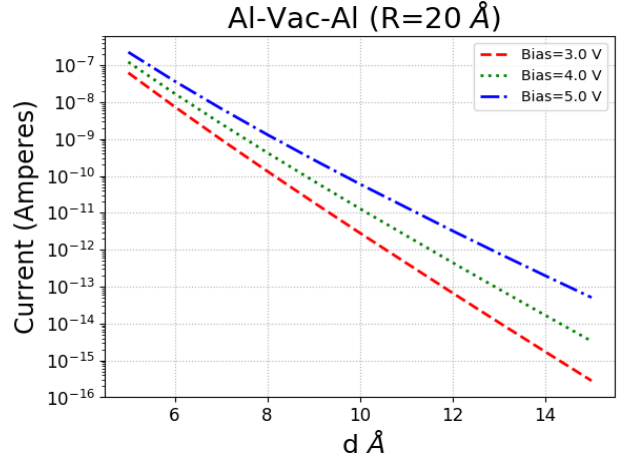


FIG. 15: Plot of Current versus Tip - Sample distance for $R = 20 \text{ Å}$ and Bias Voltage = 3, 4 and 5 V for similar electrodes

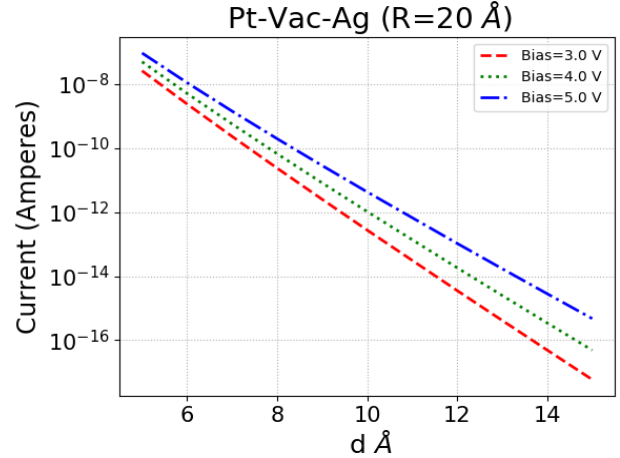


FIG. 16: Plot of Current versus Tip - Sample distance for $R = 20 \text{ Å}$ and Bias Voltage = 3, 4 and 5 V for Dissimilar electrodes

plots are for bias voltages of 3 V, 4 V and 5 V, and tip radius of curvature of $R = 20 \text{ Å}$. Therefore I is found to decrease exponentially with increasing d . This behaviour is also qualitatively reproduced by almost all calculations of tunneling current density including those that use the WKB approximation [2][11][8][25].

For fixed bias voltage V and tip sample distance d , increasing the tip radius R , leads to a flatter tip, which means that more area

in the vicinity of the center lies closer to the sample and the current density for these areas is greatly increased. Since the current I is an integral of the current density over tip area, I is expected to increase with increasing R for all V and d . Fig.17 indeed confirms this behaviour by showing how the $I - V$ curves correspond to higher currents for larger R . The general behaviour of I versus V is not much influenced by R . The Pauli Effects have

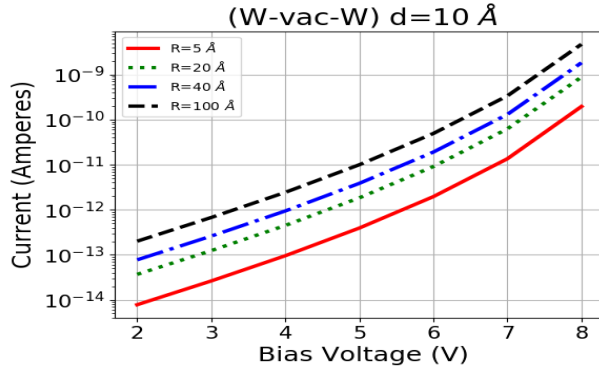


FIG. 17: Plot of Current versus Bias Voltage for $d = 10 \text{ Å}$ and $R = 5, 20, 40, 100 \text{ Å}$

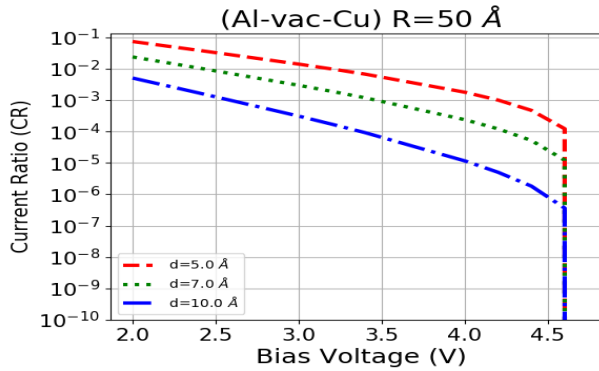


FIG. 18: Log Plot of Current Ratio (CR) as a function of Bias Voltage (2V to 5V) for $R = 50 \text{ Å}$ and $d = 5, 7, 10 \text{ Å}$.

been discussed in some detail following Figures 3,4, and 5. The effect of the third term on the tunneling currents is studied by considering the Current Ratio $CR = 1 - (I_{\text{Non-Pauli}}/I)$. Figures 18,19 show that the ratio of the third term contribution to the net tunneling current which is labelled as the CR is quite small

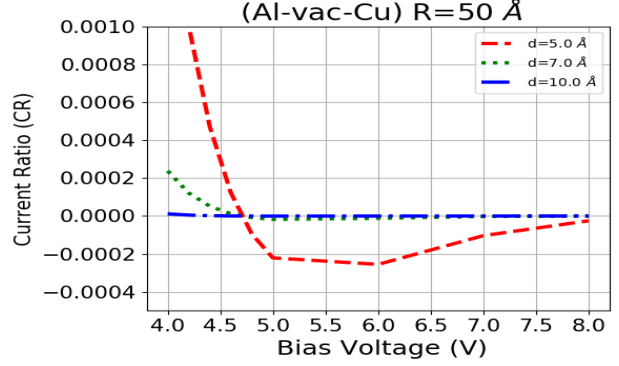


FIG. 19: Plot of Current Ratio (CR) as a function of Bias Voltage (4V to 8V) for $R = 50 \text{ Å}$ and $d = 5, 7, 10 \text{ Å}$

for all bias voltages. The value of the CR and hence the strength of the Pauli Effect decreases very fast with increasing tip-sample distance. The CR is positive for bias voltages less than $eV_b = \eta_1 - \eta_2 = 4.7 \text{ eV}$, for which voltage range $I_{\text{Net}} > I_{\text{Non-Pauli}}$ and for bias voltages greater than this value the CR is negative, implying that $I_{\text{Net}} < I_{\text{Non-Pauli}}$. The Pauli Effect has a larger magnitude at low bias voltages as compared to higher bias voltages.

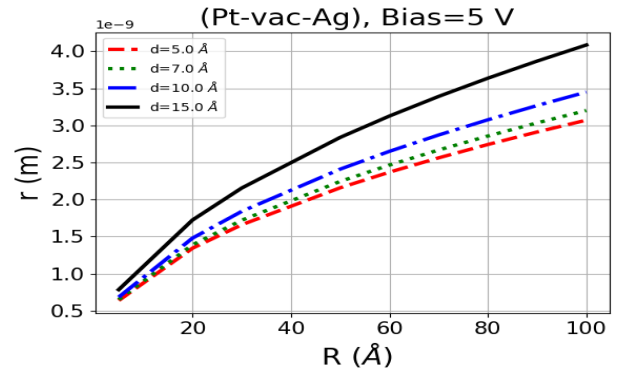


FIG. 20: Plot of r (Measure of lateral Resolution) versus R (Radius of curvature of the tip) for Bias Voltage = 5 V and Tip sample distances = 5, 7, 10, 15 Å

The ratio $\frac{I}{J_{\text{Net}}(\xi = 1)}$ gives an area σ , which can be regarded as the area of a circle of lateral resolution; *i.e.*, sample profile

features that lie within this circle would be poorly resolved. The radius $r = \sqrt{\sigma/\pi}$ of this circle would therefore be a good measure of the lateral resolution limit, and can be named as the Lateral Resolution Parameter (LRP).

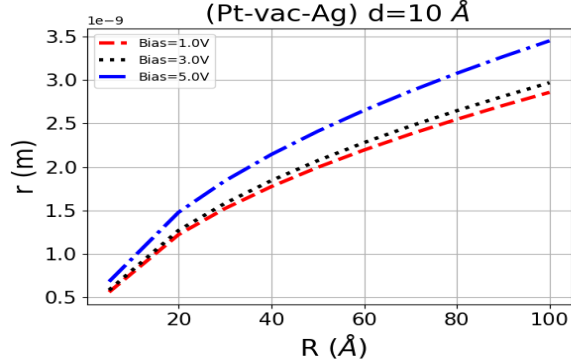


FIG. 21: Plot of r (Measure of lateral Resolution) versus R (Radius of curvature of the tip) for Tip sample distances = 10 Å and Bias Voltage=1, 3, 5 V

Fig.20 and Fig.21 show the dependence of the r (LRP) with the tip radius R which is varied from (5 Å to 100 Å). Both figures show that sharper the tip (*viz* lower the value of R), the greater is the lateral resolution (*viz* smaller the value of r). Fig.20 shows that for fixed bias the lateral resolution is degraded with increasing tip sample distance. In Fig.21 the tip sample distance is kept constant, while the bias voltage is changed. This figure shows that the lateral resolution is degraded as the bias voltage increases; which feature is found to be more pronounced at higher, rather than at lower bias voltages.

SUMMARY

The model used for calculating tunnelling current for the biased M-V-M tunnel junctions treats the effective barrier potential as a trapezoidal potential. Exact analytic expressions for the tunneling probability and current are obtained by solving the Schrödinger's equation for the trapezoidal potential, for

which the wavefunctions can be expressed in terms of Airy functions. Electrons with x-directed translational energies ranging from 0 eV to $\eta_1 + \phi_1$ contribute to tunneling.

The current is calculated for a wide range of input parameters such as tip-sample distance, bias voltage, and radius of curvature of the tip, both electrodes being at room temperature. Pauli Effects are explicitly introduced and their behaviour as a function of bias voltage and tip-sample distance is studied. A measure of lateral resolution of the tunnel junction is introduced and its behaviour as a function of tip radius of curvature for several values of bias voltage, tip sample distance is also presented.

-
- [1] G. Binnig, H. Rohrer, Ch. Gerber and E. Weibel "Surface Studies by Scanning Tunneling Microscopy" Phys. Rev. Lett. 1982, 49:57
 - [2] J. G. Simmons "Generalized Formula for the Electric Tunnel Effect between Similar Electrodes Separated by a Thin Insulating Film" Journal of applied Physics 1963, 34:1793-1803.
 - [3] Thomas E. Hartman and Jay S. Chivian "Electron Tunneling Through Thin Aluminum Oxide Films" Physical Review 1964, 134:A1094-A1101.
 - [4] J. Tersoff, D. Hamann "Theory of the scanning tunneling microscope" Phys. Rev. B 1985, 31:805-813.
 - [5] J. Bardeen "Tunneling From a Many-Particle Point Of View" Phys. Rev. Lett. 1961,6:57-59.
 - [6] J. Bardeen "Surface States and Rectification at a Metal SemiConductor Contact" Physical Review 1947, 71:717-727.
 - [7] C. Julian Chen "Role of Tip Material in Scanning Tunneling Microscopy" Mat. Res. Soc. Symp. Proc. Vol. 159. 1990.
 - [8] S. Banerjee and P. Zhang "A generalized self-consistent model for quantum tunneling

- current in dissimilar metal-insulator-metal junction" AIP Advances 9, 085302 (2019)
- [9] J. J. Saenz, R. Garcia "Near field emission Scanning tunnelling Microscopy" Appl. Phys. Lett. 1994, 65:3022-3024.
- [10] R. H. Fowler and L. Nordheim "Proc. Roy. Soc. (London) A119 (1928) 173.
- [11] J. G. Simmons "Electric Tunnel Effect between Dissimilar Electrodes Separated by a Thin Insulating Film" Journal of applied Physics 1963, 34:2581-2590.
- [12] Q.Q. Shu a, Y. Jiang b, S. Meng b, G. Lin b, W.G. Ma "Exactly solvable model for metal-insulator-metal stepped boundary tunnel junctions" Thin Solid Films 2002, 414:136–142.
- [13] C. Bracher, M. Riza, and M. Kleber "Propagator theory of scanning tunneling microscopy" Physical Review B Volume 56, Number 12
- [14] W. Ebeling, D Blaschke, R Redmer, H Reinholz, and G Ropke "The influence of Pauli blocking effects on the properties of dense hydrogen" J. Phys. A Math. Theor. 2009, 42:214033(1-8pp).
- [15] M. Abramowitz and I. A. Stegun "Handbook of Mathematical Functions": National Bureau of Standards Applied Mathematics Series-55, June 1964, Tenth Printing, December 1972, p. 446.
- [16] P.H. Cutler, Jun He, J. Miller, N. M. Miskovsky, B. Weiss and T. E. Sullivan "Theory of electron emission in high fields from atomically sharp emitters: Validity of the Fowler-Nordheim equation" Progress in Surface Science, Vol. 42, pp. 169-185 1993
- [17] S. Patil, A. Kulkarni, C.V Dharmadhikari "Study of the electrostatic force between a conducting tip in proximity with a metallic surface: Theory and experiment" Journal of Applied Phys. 2000, 88:6940-6942.
- [18] K. Date, A. Kulkarni, C.V Dharmadhikari "Force on a Conducting Tip near a Metallic Surface Coated with a Polarizable Dielectric Layer: Theory and Experiment" e-J. Surf. Sci. Nanotech. Vol. 9 (2011) 206-209
- [19] A. M. Russell "Electron Trajectories in a Field Emission Microscope" Journal of Applied Science 1962, 33:970
- [20] J. He, P.H. Cutler, N.M. Miskovsky, T.E. Feuchtwang "Derivation of the image interaction for non-planar pointed emitter geometries: application to field emission I-V characteristics" Surface Science 1991, 246: 348-364.
- [21] P. Moon and D. E. Spencer "Field Theory Handbook" 2nd Edition, Springer-Verlag Berlin Heidelberg New York (1971) Table 1.06, pp-28
- [22] P. Morse and H. Feshbach "Methods of Theoretical Physics" McGraw Hill Book Company, Inc (1953) pp-661, Volume-I
- [23] J. Aizpurua, S. P. Apell, R. Berndt "Role of tip shape in light emission from the scanning tunneling microscope" Physical Review B Volume 62, Number 3, (2000-I)
- [24] T. Xie, M. Dreyer, D. Bowen, C. Krafft "On local sensing of spin Hall effect in tungsten films by using STM-based measurements" IEEE Transactions on Nanotechnology PP(99) July 2017
- [25] W. A. Hofer, A. S. Foster, A. L. Shluger "Theories of scanning probe microscopes at the atomic scale" Reviews of Modern Physics, Volume 75, 1287, October 2003.